

Article

Bloch Surface Waves for MoS₂ Emission Coupling and Polariton Systems

Giovanni Lerario ^{1,2,*}, Dario Ballarini ¹, Lorenzo Dominici ^{1,*} , Antonio Fieramosca ^{1,3},
Alessandro Cannavale ⁴, Matthew Holwill ^{5,6}, Aleksey Kozikov ^{5,6}, Kostya S. Novoselov ^{5,6}
and Giuseppe Gigli ¹

¹ CNR-NANOTEC, Institute of Nanotechnology, via Monteroni, 73100 Lecce, Italy; dario.ballarini@gmail.com (D.B.); antonio.fieramosca@gmail.com (A.F.); giuseppe.gigli@cnr.it (G.G.)

² Laboratoire Kastler Brossel, UPMC, 4 Place Jussieu Case 74, F-75005 Paris, France

³ Dipartimento di Matematica e Fisica “Ennio De Giorgi”, Università del Salento, Via Arnesano, 73100 Lecce, Italy

⁴ Dipartimento di Scienze dell’Ingegneria Civile e dell’Architettura, Politecnico di Bari, via Orabona 4, 70125 Bari, Italy; alessandro.cannavale@poliba.it

⁵ School of Physics and Astronomy, University of Manchester, Oxford Road, Manchester M13 9PL, UK; matthew.holwill@manchester.ac.uk (M.H.); aleksey.kozikov@manchester.ac.uk (A.K.); konstantin.novoselov@manchester.ac.uk (K.S.N.)

⁶ National Graphene Institute, University of Manchester, Manchester M13 9PL, UK

* Correspondence: giovannilerario86@gmail.com (G.L.); lorenzo.dominici@gmail.com (L.D.)

Received: 30 October 2017; Accepted: 20 November 2017; Published: 24 November 2017

Abstract: Due to their extraordinary quality factor and extreme sensitivity to surface perturbations, Bloch surface waves (BSW) have been widely investigated for sensing applications so far. Over the last few years, on-chip control of optical signals through BSW has experienced a rapidly-expanding interest in the scientific community, attesting to BSW’s position at the forefront towards on-chip optical operations. The backbone of on-chip optical devices requires the choice of integrated optical sources with peculiar optic/optoelectronic properties, the efficient in-plane propagation of the optical signal and the possibility to dynamic manipulate the signal through optical or electrical driving. In this paper, we discuss our approach in addressing these requirements. Regarding the optical source integration, we demonstrate the possibility to couple the MoS₂ mono- and bi-layers emission—when integrated on top of a 1D photonic crystal—to a BSW. Afterward, we review our results on BSW-based polariton systems (BSWP). We show that the BSWPs combine long-range propagation with energy tuning of their dispersion through polariton–polariton interactions, paving the way for logic operations.

Keywords: transition metal dichalcogenides; Bloch surface wave polaritons; non-linear optics

1. Introduction

BSWs show a high quality factor and extreme sensitivity to surface perturbations combined with an easy fabrication process. Thanks to these properties, BSWs are naturally suited for label-free, fluorescence sensing applications, and, in this context, they have widely expressed their capability in the last decades [1–7]. Moreover, recent papers have investigated their potentialities for on-chip guiding and manipulation of an optical signal propagating on a 1D photonic crystal [8–14]. Several studies have followed the lead of the first seminal paper on Bloch surface wave guided modes [8], engineering the top layer of the distributed Bragg reflector (DBR) stack to achieve optical manipulation of the in-plane propagating BSW. The opening of an in-plane optical bandgap [15], surface refraction [16],

focusing and sub-wavelength focusing [9,13], and the static manipulation of optical signals [12,14] have been demonstrated in the last years, based on 2D surface optical elements.

However, all these papers show a static modification of the in-plane propagating signal and, consequently, any logic operation—which necessary involves a dynamic manipulation—is prevented. In this context, optical non-linearity has proven to be a powerful tool for achieving logic operations, both in bare optical and exciton–polariton systems [17–22].

Exciton-polaritons are quasi-particles arising from the strong coupling between excitons and photons and they behave as interacting composite bosons thanks to their half-excitonic nature. The polariton–polariton interactions—which are responsible for the Kerr non-linearity—have been used for the realization of switching [22,23], interferometers [24], and logic gates [25]. All these works have been performed at cryogenic temperatures (<10 K) in order to prevent Wannier–Mott exciton dissociation (typical of the III–V semiconductors involved in these experiments). In order to get towards realistic applications, we have investigated the possibility of strongly coupling a Bloch surface wave with Frenkel excitons, which are stable at room temperature thanks to their huge binding energy. The resulting Bloch surface wave polaritons (BSWPs) manifest very high speed (>100 $\mu\text{m}/\text{ps}$)—arising from their half-photon nature—and, consequently, macroscopic in-plane propagations. Furthermore, we have experimentally demonstrated the blueshift of the mode eigenenergies when increasing the polariton density, laying the first essential stone for the room-temperature polariton logic device's realization.

On the other hand, on-chip integration obviously requires an integrated source. Apart from the Frenkel exciton emission observed in BSWP, the integration of sources exhibiting peculiar optical and/or optoelectronic properties is tickling a new generation of optoelectronic devices [26–30]. In this context, transition metal dichalcogenide (TMDC) monolayers and bilayers have attracted an extraordinary interest in the scientific community over the last decade [28]. This research has led to the realization of photoresistors [31], transistors [32], ultrasensitive photodetectors [33], and biosensors [34], and the demonstration of the optical control of valley polarization towards spintronic devices [35,36].

The paper is organized into two main sections. In the first part, we demonstrate the coupling of the mono- and bi-layer MoS_2 emission with a BSW. The MoS_2 transition dipole moment is oriented in the plane of the device [37], allowing for a perfect matching with a TE-polarized BSW mode. Through the coupling with this high Q surface mode, the MoS_2 emission can in-plane propagate covering long distances, towards the on-chip control of the TMDC optical signals.

The second part reviews the experimental results on the strong-coupling between Frenkel exciton transitions and Bloch surface waves (i.e., BSWP), starting from the demonstration of the polariton generation to their long-range propagation and non-linear properties.

2. Coupling MoS_2 Mono- and Bi-Layer Emission

MoS_2 mono- and bi-layers are exfoliated on top of a DBR made by five pairs of $\text{TiO}_2/\text{SiO}_2$ (101 nm/138 nm) alternating layers deposited on top of a glass substrate. An additional pair of $\text{TiO}_2/\text{SiO}_2$ (14 nm/16 nm) is deposited on top of the photonic crystal in order to adapt the BSW energy dispersion to the excitonic transition of the MoS_2 mono- and bi-layer. The MoS_2 transition dipole moment (of the lowest energy excited state) lies in the plane of the device [37], therefore the MoS_2 emitted photons experience the best coupling when using a TE-polarized BSW, as in the case under our investigation.

A prism coupler in Kretschmann configuration has been used for the reflectance and emission mapping of the signal lying beyond the critical angle (Figure 1a). The energy dispersion map is obtained by projecting the back focal plane of the detection lens on an imaging CCD camera placed after a spectrometer—which allows for energy resolution. In the case of the reflection map, the excitation line consists of a white light source focused on the sample (throughout the prism side) and the reflected signal is collected using a goniometric system (Figure 1a). The photoluminescence

dispersion map uses the same detection line described above, but a 532 nm cw-laser source is focused on the mono-layer and bi-layer directly from the top deposition side.

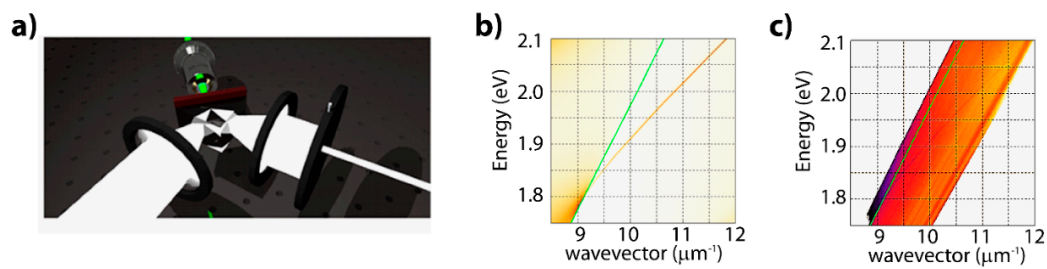


Figure 1. (a) Schematic drawing of the experimental setup used for reflectivity and emission measurements in Kretschmann configuration. (Reproduced with permission from [38], OSA Publishing, 2014). (b) TMM calculation of the BSW reflectance dispersion using a DBR composed of five pairs of $\text{TiO}_2/\text{SiO}_2$ (101 nm/138 nm) with an additional top-pair of $\text{TiO}_2/\text{SiO}_2$ (14 nm/16 nm). The light line (green line) corresponds to an angle of about 42 degrees in glass; the Bloch surface mode is the dip visible in the total internal reflection regime (yellow line on the right side to the green line). (c) Experimental reflection signal. A very shallow BSW curve is visible, in a perfect agreement with the computation in (b).

Figure 1c shows the BSW experimental dispersion in reflection configuration for the bare DBR (i.e., out of the mono- or bi-layer deposition) and Figure 1b shows the related transfer-matrix method (TMM) calculation. The bare BSW line width is below the setup energy resolution of 10 meV; we have estimated a 5 meV line width at 1.85 eV from the theoretical calculation.

A second white light source is focused through the microscope objective on the sample (similarly to the laser source), while a second camera collects the reflected signal. This second detection line allows for the visualization of the top surface (i.e., deposition side) and helps for the accurate positioning of the laser excitation ($\text{FWHM} \simeq 1 \mu\text{m}$) on the mono- or bi-layer structure. Figure 2a shows the real space map—reflectance from the top surface—of the MoS_2 mono- and bi-layers. Using this configuration, we can also detect the emission signal (when using the 532 nm laser instead of the white light source) coming from the deposition side (Figure 2b). As expected, the mono-layer emission is stronger than the bi-layer one [39].

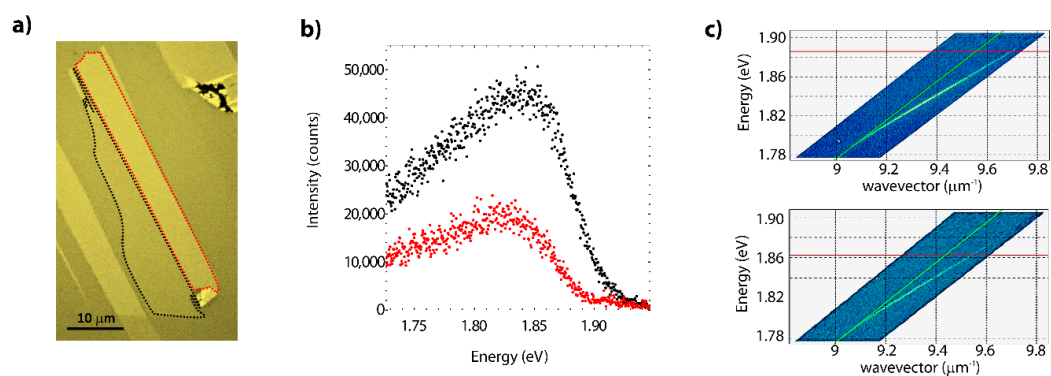


Figure 2. (a) Reflection space map (from the top side of the DBR) revealing the mono (delimited by black dashed line) and bilayer (delimited by red dashed line) of MoS_2 . (b) Emission signals of mono (black dots) and bilayer (red dots) detected from the top of the DBR. (c) Monolayer (upper panel) and bilayer (lower panel) dispersion emission coupled to the BSW (i.e., detected from the prism side and across the total internal reflection regime). The green line defines the lightline dispersion, and the red line the excitonic absorption peak energy.

When detecting the signals coming from the substrate side (i.e., prism coupler side), the monolayer and bilayer photoluminescence coupled to the Bloch surface mode is observed (Figure 2b,c, respectively). Because of the BSWs' high sensitivity to surface refractive index variations, we would expect a perturbation of the mono- and bi-layer dispersion with respect to the bare BSW curve. In the present case, we observe identical dispersions for all these three signals, because most of the emission is propagating out of the MoS₂ deposition after its generation, coupling with the BSW of the bare DBR.

3. Bloch Surface Wave Polaritons

In this second section, we will review the recent results on Bloch surface wave exciton–polaritons (BSWPs). The photon–exciton strong coupling leads to the hybridization of the bare components with the consequent generation of two hybrid eigenmodes, the upper and lower polariton branches.

A first theoretical proposal in 2011 [40], predicted the generation of BSWP using GaAs quantum wells deposited on top of a DBR. The first experimental demonstration of the formation of a BSWP was simultaneously obtained in 2014 from two different research teams [38,41]. In both these experimental papers—different from the first theoretical proposal—the excitonic medium is an organic layer. This choice comes with the benefit to work at room temperature, where the oil immersion techniques (useful for the extraction of the signals beyond the critical angle) are available. Indeed, Wannier–Mott excitons (typical of III–V semiconductors, including GaAs) dissociate at room temperature because of their weak electron–hole binding energy, while excitons in organic materials (Frenkel excitons) have a strong binding energy, making them stable also at high temperature. Furthermore, considering that the exciton–photon coupling strength increases with increasing exciton oscillator strength, the huge absorption coefficient ($>100,000\text{ cm}^{-1}$) of some of these organic materials—makes them perfect candidates for the obtainment of the strong coupling regime.

In the experiments performed by our team [38], a 20 nm thick layer is deposited on top of a DBR—identical to the DBR described in the previous section—via spin coating technique starting from a blend of TDBC:PVA (1:1 weight ratio) dissolved in a mixture of methanol:water (1:1 volume ratio). Using the same setup reported in the previous experiments on MoS₂, emission and reflection signals lying in total internal reflection regimes are collected. The pinhole positioned at the back focal plane of the detection lens allows for the scan of the dispersion map with an angular resolution of 0.2° .

The TDBC is an organic dye with extremely huge extinction coefficient deriving from its J-aggregating property. The PVA is a polymer with a large energy bandgap (about 5.3 eV), used as a matrix to obtain an homogeneous distribution of the aggregates within the excitation area and to avoid the formation of big TDBC aggregates—which can drastically reduce the quality of the BSW mode.

Scanning the back focal plane of the detection lens with the pinhole, two polaritonic branches are clearly observed when approaching the TDBC exciton transition. Figure 3a shows the typical anticrossing behavior of a polariton system in both reflection and emission measurements. The Rabi splitting is about 45 nm and the FWHM of the polariton modes at the anticrossing point is 14 meV. Figure 3b shows experimental data (black dots) superimposed to the theoretical dispersion map (TMM calculations).

The interest for these particular exciton–polariton modes derives from the fact that these hybrid states exhibit macroscopic propagation. Indeed, both metal-based surface and planar microcavity modes are affected by intrinsic losses, which limit the quasi-particle propagation length. The main drawback of the first one is the metal dissipation, while the low group velocity (about 1% of light speed at maximum) is the main limitation in the propagation of planar microcavity polaritons. On the contrary, BSWPs exhibit group speed which can be higher than 50% speed of light—which is also much larger than the light speed in the excitonic medium—and very low dissipations—thanks to the fact that the supporting structure is almost completely made by dielectric materials. These properties have been accurately investigated and reported in the paper “High Speed Flow of Interacting Organic

Polaritons" (G. Lerario et al. *Light: Science & Applications* 2017, 6, e16212) [42]. Hereafter, we will reassume the main findings.

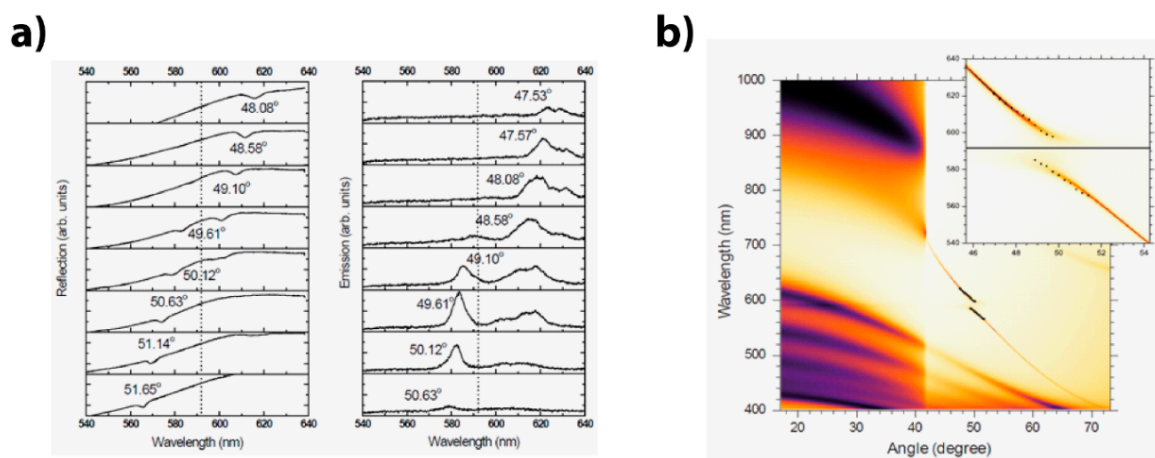


Figure 3. (a) Reflectivity (left) and photoluminescence (right) spectra taken at different angles of incidence with respect to the normal to the sample inside prism. The dashed line is the molecule absorption peak position [38]. (b) Experimental data (dots) superimposed to the theoretical calculation of the reflectivity as a function of wavelength and angle of incidence. The anticrossing behavior (distinctive of strong coupled systems) is evidenced in the inset (the horizontal black line is the exciton transition). Reproduced with permission from G. Lerario et al., *Optics Letters* 39 (7), 2068, © [Optical Society of America], 2014 [38].

The unavoidable inhomogeneity of the spin coated TDBC aggregates limits the polariton lifetime (because of scattering out of the BSWP mode), and consequently their propagation in the plane of the device. In order to overcome this drawback, a thermally evaporable organic molecule has been used, which guarantees a high homogeneity of the deposition. A 35 nm thick layer of Lumogen Red 305 has been deposited on a photonic crystal (seven couples of $\text{TiO}_2/\text{SiO}_2$, 85 nm/120 nm, respectively) obtaining a Rabi splitting of 186 meV.

Instead of the prism-coupler, a leakage radiation microscope is necessary when detecting the spatial distribution of the polaritons in the plane of the device. This detection system consists of an oil immersion microscope objective placed at the substrate side in order to extract signals lying in the total internal reflection regime. An out-of-resonance excitation source (532 nm) is focused on the sample surface by means of a second microscope objective placed at the deposition side (Figure 4a). The sketch of the optical setup is in Figure 4a.

The overall in-plane propagation length of the BSWP is about 120 μm . Both a record quality factor and huge group velocity allow for this extremely long propagation distance, which is comparable to the best inorganic microcavity samples, and on the contrary has been achieved using an easy fabrication process and working at room temperature. In particular, the Q-factor is about 3000, which is about 10-times larger than typical values obtained in organic planar microcavities, where the deposition process of a second DBR on top of the organic layer drastically reduces the quality of the polariton modes. On the other hand, the group velocity (around 150 $\mu\text{m}/\text{ps}$ at the maximum emission intensity) of the BSWP is about 10-times larger than the maximum velocity achievable in typical planar microcavities.

It is important to note that the observed propagation length is now limited by the extraction of the signal through the oil immersion objective (i.e., such leakage is contributing to the effective total loss), while—differently from planar microcavity modes—the surface flow can last for longer distances if not extracted.

Furthermore, we have studied the polariton–polariton interactions via resonant generation of polaritons. The excitation beam (35 fs pulsed laser) is focused on the sample through the oil immersion objective also used for the detection (Figure 4a). Using this configuration and working in total internal reflection regime, the detected signal is the reflection of the sample. The slit (S2 in Figure 4) along the detection line selects the excitation spot area, cutting off the propagating signal. Because of this selection, the BSWP appears as a dip in the dispersion map (Figure 4c, top left panel). When increasing the pump power, the polariton resonance blueshifts. Figure 4c (bottom left panel) shows the TMM calculations (solid lines) of the BSWP dispersion when considering an exciton energy of 2.13 eV (blue) and a blue-shifted (8 meV) exciton (red). They perfectly match the experimental values for $150 \mu\text{J cm}^{-2}$ and 10 mJ cm^{-2} , respectively. The linear dependence with the exciton fraction (Figure 4, bottom right) demonstrates that the blueshift is originated by the polariton–polariton repulsive interaction (estimated interaction constant $g = 10^{-3} \mu\text{eV } \mu\text{m}^2$).

As shown in Figure 4c (top right panel), the mode blueshift exceeds the mode linewidth, which is a fundamental requirement for the realization of polariton devices, such as switches and logic gates.

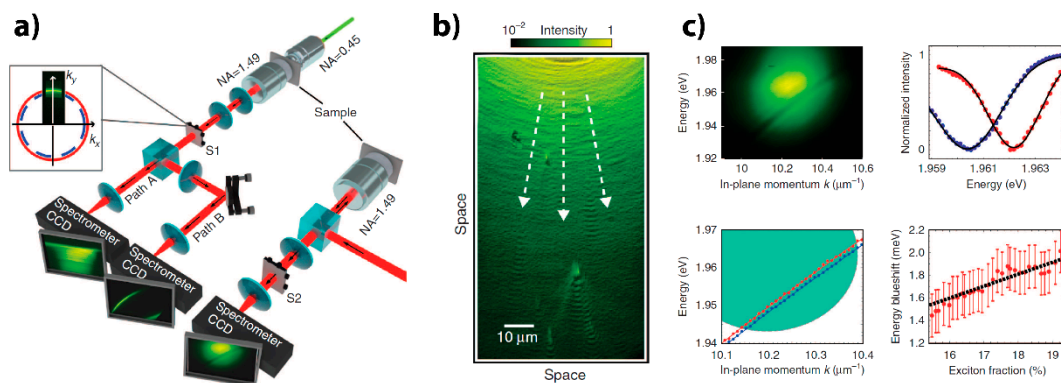


Figure 4. (a) In the upper part, a sketch of the leakage radiation microscope setup in a non-resonant configuration. The excitation source (a cw laser at 2.33 eV) is focused on the sample from the organic deposition side. The emission is collected through a microscope objective with NA = 1.49. In the bottom part, a sketch of the resonant configuration. The excitation laser (100-fs laser pulse) is energetically matched with the BSWP mode and focused through the oil immersion objective. (b) Space map of the non-resonant excited polariton emission; the white arrows are a guide for the eye indicating the radial directions starting from the excitation spot (i.e., BSWP propagation direction). (c) BSWP nonlinearities. (top left) Bare experimental data of the BSWP dispersion in reflectance configuration at $150 \mu\text{J cm}^{-2}$ pumping energy. (top right) Energy-resolved signal at in-plane wavevector $k = 10.34 \mu\text{m}^{-1}$ under $150 \mu\text{J cm}^{-2}$ and 10 mJ cm^{-2} excitation energy densities (blue and red dots, respectively), showing the blueshift of the BSWP resonance. (bottom left) Experimental BSWP dispersions with $150 \mu\text{J cm}^{-2}$ (blue) and 10 mJ cm^{-2} (red) resonant pump pulse. The green ellipse depicts the resonant laser central position and size in the energy–momentum domain (FWHM circle). (bottom right) The expected blueshift as a function of the excitonic fraction (black dashed line) fits the experimental results (red dots) for a bare exciton blueshift of 8 meV. (Adapted with permission from [42], Nature Publishing Group, 2017)

4. Conclusions

In conclusion, we have demonstrated the emission coupling of the MoS₂ mono- and bi-layer emission with a high Q surface mode. The MoS₂ transition dipoles are oriented in the plane of the 1D photonic crystal, which allows for a perfect matching with the TE-polarized BSW. Coupled mono- and bi-layer emission have the same energy dispersion, which is also identical to the BSW mode dispersion of the bare DBR. Considering the high sensitivity of the BSW to surface perturbations, this result suggests that the coupled emission is mostly propagating out of the small MoS₂ stripe (coupling

with the BSW of the bare DBR). These results pave the way for an on-chip propagation control and manipulation of the TMDC emission signals.

In the second section, we have reviewed the main results obtained by our group in the field of BSWP. Soon after the first demonstration of the strong coupling between BSW and Frenkel excitons at room temperature, we have demonstrated the in-plane BSWP propagation for macroscopic distances. This result has been achieved thanks to the extraordinary speed of this particular polariton mode, which is close to 50% of the speed of light. Furthermore, we proved the first nonlinear BSWP, which is the dispersion blueshift when increasing the polariton density due to polariton–polariton interactions, demonstrating the extraordinary potential of this system in the field of optical logic devices.

Acknowledgments: The authors would like to thank Daniele Sanvitto and Milena De Giorgi for useful discussions and scientific support. This work has been funded by the MIUR project Beyond Nano and the ERC project POLAFLOW (Grant No. 308136).

Author Contributions: G.L., D.B., L.D. and K.S.N. conceived and designed the experiments; G.L. and A.F. performed the experiments; A.C., G.L., A.F., M.H., A.K. and K.S.N. provided the sample; G.L. analyzed the data; all the authors contributed to the data discussion; G.L. wrote the paper with contributions from all the authors.

Conflicts of Interest: The authors declare no conflict of interest.

References

1. Liedberg, B.; Nylander, C.; Lundström, I. Biosensing with Surface Plasmon Resonance—How It All Started. *Biosens. Bioelectron.* **1995**, *10*, 1–9. [[CrossRef](#)]
2. Sinibaldi, A.; Danz, N.; Descrovi, E.; Munzert, P.; Schulz, U.; Sonntag, F.; Dominici, L.; Michelotti, F. Direct comparison of the performance of Bloch surface wave and surface plasmon polariton sensors. *Sens. Actuators B Chem.* **2012**, *174*, 292–298. [[CrossRef](#)]
3. Sinibaldi, A.; Sampaoli, C.; Danz, N.; Munzert, P.; Sonntag, F.; Centola, F.; Occhicone, A.; Tremante, E.; Giacomini, P.; Michelotti, F. Bloch Surface Waves Biosensors for High Sensitivity Detection of Soluble ERBB2 in a Complex Biological Environment. *Biosensors* **2017**, *7*, 33. [[CrossRef](#)] [[PubMed](#)]
4. Paeder, V.; Musi, V.; Hvozdar, L.; Herminjard, S.; Herzig, H.P. Detection of protein aggregation with a Bloch surface wave based sensor. *Sens. Actuators B Chem.* **2011**, *157*, 260–264. [[CrossRef](#)]
5. Kang, X.-B.; Wen, L.-W.; Wang, Z.-G. Design of guided Bloch surface wave resonance bio-sensors with high sensitivity. *Opt. Commun.* **2017**, *383*, 531–536. [[CrossRef](#)]
6. Li, Y.; Yang, T.; Song, S.; Pang, Z.; Du, G.; Han, S. Phase properties of Bloch surface waves and their sensing applications. *Appl. Phys. Lett.* **2013**, *103*, 41116. [[CrossRef](#)]
7. Sinibaldi, A.; Descrovi, E.; Giorgis, F.; Dominici, L.; Ballarini, M.; Mandracci, P.; Danz, N.; Michelotti, F. Hydrogenated amorphous silicon nitride photonic crystals for improved-performance surface electromagnetic wave biosensors. *Biomed. Opt. Express* **2012**, *3*, 2405–2410. [[CrossRef](#)] [[PubMed](#)]
8. Descrovi, E.; Sfez, T.; Quaglio, M.; Brunazzo, D.; Dominici, L.; Michelotti, F.; Herzig, H.P.; Martin, O.J.; Giorgis, F. Guided Bloch Surface Waves on Ultrathin Polymeric Ridges. *Nano Lett.* **2010**, *10*, 2087–2091. [[CrossRef](#)] [[PubMed](#)]
9. Kim, M.-S.; Vosoughi Lahijani, B.; Descharmes, N.; Straubel, J.; Negredo, F.; Rockstuhl, C.; Hayrinen, M.; Kuittinen, M.; Roussey, M.; Herzig, H.P. Subwavelength Focusing of Bloch Surface Waves. *ACS Photonics* **2017**, *4*, 1477–1483. [[CrossRef](#)]
10. Kovalevich, T.; Boyer, P.; Suarez, M.; Salut, R.; Kim, M.S.; Herzig, H.P.; Bernal, M.P.; Grosjean, T. Polarization controlled directional propagation of Bloch surface wave. *Opt. Express* **2017**, *25*, 5710–5715. [[CrossRef](#)] [[PubMed](#)]
11. Dubey, R.; Lahijani, B.V.; Barakat, E.; Häyrynen, M.; Roussey, M.; Kuittinen, M.; Herzig, H.P. Near-field characterization of a Bloch-surface-wave-based 2D disk resonator. *Opt. Lett.* **2016**, *41*, 4867–4870. [[CrossRef](#)] [[PubMed](#)]
12. Yu, L.; Barakat, E.; Sfez, T.; Hvozdar, L.; Di Francesco, J.; Herzig, H.P. Manipulating Bloch surface waves in 2D: A platform concept-based flat lens. *Light Sci. Appl.* **2014**, *3*, e124. [[CrossRef](#)]

13. Angelini, A.; Barakat, E.; Munzert, P.; Boarino, L.; De Leo, N.; Enrico, E.; Giorgis, F.; Herzig, H.P.; Pirri, C.F.; Descrovi, E. Focusing and Extraction of Light mediated by Bloch Surface Waves. *Sci. Rep.* **2014**, *4*, 5428. [[CrossRef](#)] [[PubMed](#)]
14. Yu, L.; Barakat, E.; Di Francesco, J.; Herzig, H.P. Two-dimensional polymer grating and prism on Bloch surface waves platform. *Opt. Express* **2015**, *23*, 31640–31647. [[CrossRef](#)] [[PubMed](#)]
15. Sfez, T.; Descrovi, E.; Dominici, L.; Nakagawa, W.; Michelotti, F.; Giorgis, F.; Herzig, H.P. Near-field analysis of surface electromagnetic waves in the bandgap region of a polymeric grating written on a one-dimensional photonic crystal. *Appl. Phys. Lett.* **2008**, *93*, 61108. [[CrossRef](#)]
16. Sfez, T.; Descrovi, E.; Yu, L.; Quaglio, M.; Dominici, L.; Nakagawa, W.; Michelotti, F.; Giorgis, F.; Herzig, H.P. Two-dimensional optics on silicon nitride multilayer: Refraction of Bloch surface waves. *Appl. Phys. Lett.* **2010**, *96*, 151101. [[CrossRef](#)]
17. Andalib, P.; Granpayeh, N. All-optical ultracompact photonic crystal AND gate based on nonlinear ring resonators. *JOSA B* **2009**, *26*, 10–16. [[CrossRef](#)]
18. Liu, Y.; Qin, F.; Meng, Z.M.; Zhou, F.; Mao, Q.H.; Li, Z.Y. All-optical logic gates based on two-dimensional low-refractive-index nonlinear photonic crystal slabs. *Opt. Express* **2011**, *19*, 1945–1953. [[CrossRef](#)] [[PubMed](#)]
19. Noshad, M.; Abbasi, A.; Ranjbar, R.; Kheradmand, R. Novel All-Optical Logic Gates Based on Photonic Crystal Structure. *J. Phys. Conf. Ser.* **2012**, *350*, 12007. [[CrossRef](#)]
20. Almeida, V.R.; Barrios, C.A.; Panepucci, R.R.; Lipson, M. All-optical control of light on a silicon chip. *Nature* **2004**, *431*, 1081–1084. [[CrossRef](#)] [[PubMed](#)]
21. Pöllinger, M.; Rauschenbeutel, A. All-optical signal processing at ultra-low powers in bottle microresonators using the Kerr effect. *Opt. Express* **2010**, *18*, 17764–17775. [[CrossRef](#)] [[PubMed](#)]
22. Amo, A.; Liew, T.C.H.; Adrados, C.; Houdré, R.; Giacobino, E.; Kavokin, A.V.; Bramati, A. Exciton–polariton spin switches. *Nat. Photonics* **2010**, *4*, 361–366. [[CrossRef](#)]
23. Gao, T.; Eldridge, P.S.; Liew, T.C.H.; Tsintzos, S.I. Polariton condensate transistor switch. *Phys. Rev. B* **2012**, *85*, 235102. [[CrossRef](#)]
24. Sturm, C.; Tanese, D.; Nguyen, H.S.; Flayac, H.; Galopin, E.; Lemaître, A.; Sagnes, I.; Solnyshkov, D.; Amo, A.; Malpuech, G.; et al. All-optical phase modulation in a cavity-polariton Mach–Zehnder interferometer. *Nat. Commun.* **2014**, *5*, 3278. [[CrossRef](#)] [[PubMed](#)]
25. Ballarini, D.; De Giorgi, M.; Cancellieri, E.; Houdré, R.; Giacobino, E.; Cingolani, R.; Bramati, A.; Gigli, G.; Sanvitto, D. All-optical polariton transistor. *Nat. Commun.* **2013**, *4*, 1778. [[CrossRef](#)] [[PubMed](#)]
26. Amlani, I.; Orlov, A.O.; Toth, G.; Bernstein, G.H.; Lent, C.S.; Snider, G.L. Digital Logic Gate Using Quantum-Dot Cellular Automata. *Science* **1999**, *284*, 289–291. [[CrossRef](#)] [[PubMed](#)]
27. Kim, W.Y.; Kim, H.D.; Kim, T.T.; Park, H.S.; Lee, K.; Choi, H.J.; Lee, S.H.; Son, J.; Park, N.; Min, B. Graphene–ferroelectric metadevices for nonvolatile memory and reconfigurable logic-gate operations. *Nat. Commun.* **2016**, *7*, 10429. [[CrossRef](#)] [[PubMed](#)]
28. Wang, Q.H.; Kalantar-Zadeh, K.; Kis, A.; Coleman, J.N.; Strano, M.S. Electronics and optoelectronics of two-dimensional transition metal dichalcogenides. *Nat. Nanotechnol.* **2012**, *7*, 699–712. [[CrossRef](#)] [[PubMed](#)]
29. Sordan, R.; Traversi, F.; Russo, V. Logic gates with a single graphene transistor. *Appl. Phys. Lett.* **2009**, *94*, 73305. [[CrossRef](#)]
30. Chen, W.; Yang, L.; Wang, P.; Zhang, Y.; Zhou, L.; Yang, T.; Wang, Y.; Yang, J. Electro-optical logic gates based on graphene–silicon waveguides. *Opt. Commun.* **2016**, *372*, 85–90. [[CrossRef](#)]
31. Yin, Z.; Li, H.; Li, H.; Jiang, L.; Shi, Y.; Sun, Y.; Lu, G.; Zhang, Q.; Chen, X.; Zhang, H. Single-Layer MoS₂ Phototransistors. *ACS Nano* **2012**, *6*, 74–80. [[CrossRef](#)] [[PubMed](#)]
32. Radisavljevic, B.; Radenovic, A.; Brivio, J.; Giacometti, V.; Kis, A. Single-layer MoS₂ transistors. *Nat. Nanotechnol.* **2011**, *6*, 147–150. [[CrossRef](#)] [[PubMed](#)]
33. Lopez-Sanchez, O.; Lembke, D.; Kayci, M.; Radenovic, A.; Kis, A. Ultrasensitive photodetectors based on monolayer MoS₂. *Nat. Nanotechnol.* **2013**, *8*, 497–501. [[CrossRef](#)] [[PubMed](#)]
34. Zeng, S.; Hu, S.; Xia, J.; Anderson, T.; Dinh, X.Q.; Meng, X.M.; Coquet, P.; Yong, K.T. Graphene–MoS₂ Hybrid Nanostructures enhanced Surface Plasmon Resonance Biosensors. *Sens. Actuators B Chem.* **2015**, *207*, 801–810. [[CrossRef](#)]
35. Zeng, H.; Dai, J.; Yao, W.; Xiao, D.; Cui, X. Valley polarization in MoS₂ monolayers by optical pumping. *Nat. Nanotechnol.* **2012**, *7*, 490–493. [[CrossRef](#)] [[PubMed](#)]

36. Mak, K.F.; He, K.; Shan, J.; Heinz, T.F. Control of valley polarization in monolayer MoS₂ by optical helicity. *Nat. Nanotechnol.* **2012**, *7*, 494–498. [[CrossRef](#)] [[PubMed](#)]
37. Schuller, J.A.; Karaveli, S.; Schiros, T.; He, K.; Yang, S.; Kyriassis, I.; Shan, J.; Zia, R. Orientation of luminescent excitons in layered nanomaterials. *Nat. Nanotechnol.* **2013**, *8*, 271–276. [[CrossRef](#)] [[PubMed](#)]
38. Lerario, G.; Cannavale, A.; Ballarini, D.; Dominici, L.; De Giorgi, M.; Liscidini, M.; Gerace, D.; Sanvitto, D.; Gigli, G. Room temperature Bloch surface wave polaritons. *Opt. Lett.* **2014**, *39*, 2068. [[CrossRef](#)] [[PubMed](#)]
39. Mak, K.F.; Lee, C.; Hone, J.; Shan, J.; Heinz, T.F. Atomically Thin MnS₂: A New Direct-Gap Semiconductor. *Phys. Rev. Lett.* **2010**, *105*, 136805. [[CrossRef](#)] [[PubMed](#)]
40. Liscidini, M.; Gerace, D.; Sanvitto, D.; Bajoni, D. Guided Bloch surface wave polaritons. *Appl. Phys. Lett.* **2011**, *98*, 121118. [[CrossRef](#)]
41. Pirotta, S.; Patrini, M.; Liscidini, M.; Galli, M.; Dacarro, G.; Canazza, G.; Guizzetti, G.; Comoretto, D.; Bajoni, D. Strong coupling between excitons in organic semiconductors and Bloch surface waves. *Appl. Phys. Lett.* **2014**, *104*, 51111. [[CrossRef](#)]
42. Lerario, G.; Ballarini, D.; Fieramosca, A.; Cannavale, A.; Genco, A.; Mangione, F.; Gambino, S.; Dominici, L.; De Giorgi, M.; Gigli, G.; et al. High-speed flow of interacting organic polaritons. *Light Sci. Appl.* **2017**, *6*, e16212. [[CrossRef](#)]



© 2017 by the authors. Licensee MDPI, Basel, Switzerland. This article is an open access article distributed under the terms and conditions of the Creative Commons Attribution (CC BY) license (<http://creativecommons.org/licenses/by/4.0/>).